# Discrete element modeling of the anchor-tip interactions during self-penetration of a bio-inspired probe

Modélisation par éléments discrets des interactions ancre-pointe lors de l'auto-pénétration d'une sonde bio-inspirée

# Yuyan Chen, Alejandro Martinez, Jason DeJong

Department of Civil and Environmental Engineering, University of California Davis, United States, yych@ucdavis.edu

ABSTRACT: Site characterization activities, such as Cone Penetration Testing (CPT), Pressuremeter Testing (PMT), and Dilatometer Testing (DMT), can be compromised due to challenges associated with equipment mobilization. This situation is common at locations such as the toe of dams, dense urban environments, deep water, and extraterrestrial bodies. This research uses bio-inspiration to develop a probe that can penetrate itself into the subsurface, eliminating the need for a drill rig to provide the reaction mass. This probe uses an adaptation employed by razor clams, worms, and caecilians where a body section is radially expanded to form an anchor which generates the reaction force needed to penetrate the soil. This paper presents a Discrete Element Modeling (DEM) study of the self-penetration process of this probe. Analysis of soil stress states indicates that the probe configuration influences its self-penetration ability. Specifically, the distance between the anchor and the tip affects the interaction between these probe parts due to principal stress rotation and arching. The results indicate that self-penetration is achievable in medium-dense coarse-grained soil by bio-inspired probes with smaller anchor-tip spacings and provide useful information for the design of future probe prototypes.

RÉSUMÉ: Les activités de caractérisation du site, telles que les CPT, PMT et DMT, peuvent être compromises en raison des défis associés à la mobilisation des équipements. Cette situation est courante dans des endroits tels que le pied des barrages, les environnements urbains denses, les eaux profondes et les corps extraterrestres. Cette recherche utilise la bio-inspiration pour développer une sonde conceptuelle qui peut se pénétrer dans le sous-sol, éliminant le besoin d'une plate-forme pour fournir une masse de réaction. Cette sonde utilise une adaptation employée par les couteaux, les vers et les caecilians où une section du corps est d'abord expansée radialement pour former une ancre, générant la force de réaction nécessaire pour surmonter la résistance à la pénétration. Cet article présente une étude DEM qui modélise le processus de pénétration de cette sonde. L'analyse des états de stress du sol indique que la configuration de la sonde influence sa capacité d'auto-creusage. Plus précisément, la distance entre l'ancre et la pointe affecte l'interaction entre ces pièces de sonde en raison de la rotation de contrainte principale et de la cambrure du sol. Les résultats indiquent que l'auto-pénétration est réalisable dans un sol moyennement dense à gros grains par la sonde bio-inspirée.

KEYWORDS: discrete element modeling, bio-inspiration, self-penetration, site investigation.

### 1 INTRODUCTION

In current geotechnical engineering, soil penetration is an energy-intensive process that is usually achieved using large equipment. For example, drill rigs are needed to provide reaction mass for in-situ CPT, PMT, and DMT testing, hammers and cranes are usually required for pile driving, and tunnel boring machines (TBMs) are used for underground excavation and tunneling. The need for large equipment can cause accessibility challenges in sites with limited accessibility (e.g. Mayne 2007), such as the toe of a dam, congested urban areas, forested areas, deep water, and extraterrestrial bodies. The use of large equipment is also responsible for a large portion of the negative environmental impacts during site investigation activities (Raymond et al. 2020, Purdy et al. 2020).

Soil penetration is also a common problem for organisms that live underground. Different from the human methods described above, organisms have developed efficient soil penetration strategies. For example, earthworms use peristalsis (e.g. Sadava et al. 2009) and caecilians and razor clams use the internal concertina and dual anchor strategies, respectively (e.g. Gans 1973; Dorgan 2015), as their principal modes of burrowing locomotion. One common feature of these soil penetration strategies is that they involve radial expansion of a body part to generate anchorage to subsequently overcome the soil penetration resistance generated during longitudinal advancement. Here, this is referred to as the 'anchor-tip' strategy.

The field of bio-inspired geotechnics has received significant attention in recent years, focused on applying biological strategies and principles to develop efficient and environmental-friendly solutions for engineering problems (Martinez et al. 2021). Examples of bio-inspired geotechnics research include

experimental and numerical studies on the performance of self-penetrating probes and robots in different soil conditions (e.g. Cortes and John 2018; Khosravi et al. 2018; Martinez et al. 2020; Tao et al. 2020; Chen et al. 2021; Borela et al. 2021), laboratory and geotechnical centrifuge investigations on snakeskin-inspired surfaces and piles that develop directional-dependent skin friction (e.g. Martinez et al. 2019; O'Hara and Martinez 2020; Stutz and Martinez 2021), and laboratory and field investigation on tree-root inspired foundations and anchors (e.g. Mallett et al. 2018; Meijer et al. 2019; Burrall et al. 2020).

This paper presents DEM simulations of the self-penetration process of a bio-inspired probe that uses the 'anchor-tip' strategy. This probe consists of a radially-expanding section (i.e. anchor) which generates anchorage reaction forces and an axially-elongating section (i.e. tip) which mobilizes resistance forces during soil penetration. Emphasis is placed herein on the effect of the distance between the probe's tip and the anchor on the mobilization and evolution of the penetration resistance and anchorage forces. Global-scale analysis of the forces acting on the probe allows for investigation of the favorable anchor locations that enable self-penetration (i.e. the ability to advance the tip with the generated anchorage forces), while meso-scale analysis of the state of stresses within the soil reveals the mechanisms that give rise to the interactions between the tip and the anchor.

## 2 DEM MODEL

The discrete element modeling (DEM) simulations of this investigation are performed using the PFC 3D software (Itasca). The DEM model consists of a cylindrical calibration chamber

that applies constant boundary stresses, a bio-inspired probe, and particles, as described below.

#### 2.1 Model parameters and calibrations

The cylindrical calibration chamber has a dimeter ( $D_{chamber}$ ) of 0.7 m and a height (H<sub>chamber</sub>) of 1.2 m (Figure 1a). The chamber consists of a top wall that applies a constant vertical pressure, and 12 radial walls that apply constant radial pressure. A servocontrol algorithm is used to achieve an effective overburden stress of 100 kPa with  $K_0$ =0.5 condition (i.e. the effective radial stress of 50 kPa). The probe has a diameter ( $D_{probe}$ ) of 0.044 m and an apex angle of 60°, which is equivalent to the diameter of a 15 cm<sup>2</sup> CPT probe. The specimen contained within the chamber consists of about 200,000 spherical particles with a density of 2650 kg/m<sup>3</sup>. The particles are upscaled to reduce the computational time; the particles have a mean size  $(D_{50})$  of 0.0144 m and a coefficient of uniformity (C<sub>U</sub>) of 1.2. The chamber-to-probe diameter (D<sub>chamber</sub> /D<sub>probe</sub>) and the probe-toparticle diameter ( $D_{probe}$  / $D_{50}$ ) are 15.9 and 3.1 respectively. While these values are smaller than typical values in experimental investigations, authors such as Khosravi et al. (2020), Chen et al. (2021), Ciantia et al. (2016), Zhang et al. (2019), and Arroyo et al. (2011) have shown that these D<sub>chamber</sub>/D<sub>probe</sub> and D<sub>probe</sub>/D<sub>50</sub> values successfully eliminate potential boundary and particle size effects in DEM simulations.

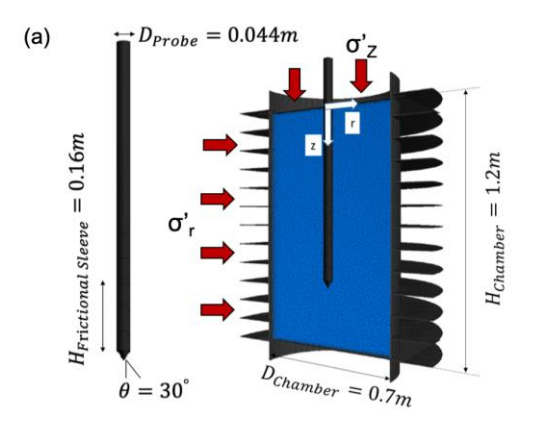
The inter-particle and particle-object contacts are modeled with the linear contact model with rolling resistance; the addition of rolling resistance enables the proper simulation of the response of sub-rounded to sub-angular soil (e.g. Wensrich and Katterfeld 2012). The main simulation parameters are shown in Figure 1b. The normal stiffness of particle ( $k_n$ ) is proportional to the particle diameter (d), with the  $k_n/d$  ratio being  $10^8$  N/m<sup>2</sup>. The sliding and rolling friction coefficients are both 0.4. The particle-probe friction coefficient is 0.3 and the particle-chamber wall friction coefficient is set as 0.1. All the specimens tested in this investigation were initially  $K_0$ -consolidated to an initial void ratio of 0.61. A detailed description of the simulation configuration and parameters can be found in Chen et al. (2021).

To investigate the behavior of the simulated particle assemblies and to verify that this behavior is representative of typical sands, a series of triaxial simulations were performed. Select results of the triaxial simulations are shown in Figures 1c and 1d for specimens subjected to confining stresses of 5, 25, 100, and 400 kPa. The triaxial response shows the expected trends, including the increase in mobilized deviatoric stress and decrease in dilatancy (i.e. smaller volumetric strain) as the confining stress is increased. Other trends include the decrease in the peak value of the deviatoric to mean stress ratio (q/p') with increasing confining stress, and the mobilization of a unique, critical state q/p' value for all confining stress levels. The simulations indicate that the particle assemblies mobilize a critical state friction angle of 36.0°. Additionally, Chen et al. (2021) presents the results of a series of CPT simulations which show that the DEM model successfully reproduces trends from field in-situ tests in medium-dense sands, including the increase in penetration resistance  $(q_c)$  and sleeve friction  $(f_s)$ measurements with increasing overburden pressure as well as Soil Behavior Type (SBT) classifications of clean sands.

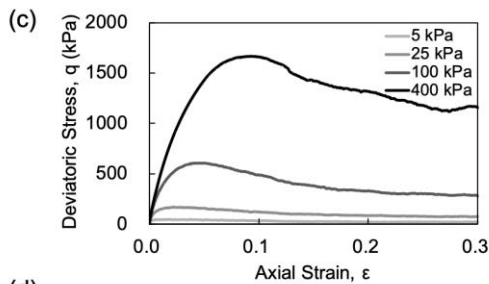
## 2.2 Self-penetration process and probe configuration

This investigation has the goal of simulating one cycle of the self-penetration process at a constant overburden stress level equivalent to that applied by 10 m of saturated soil. It should be noted that in the field applications, multiple cycles would be needed for the probe to reach this depth. Therefore, in this study, an initial direct penetration is simulated to achieve a probe embedment which allows for the subsequent probe anchorage. This initial process is termed the cone penetration (CP) stage,

which is followed by the anchor expansion (AE) and self-penetration (SP) stages (Figure 2). This paper focuses on the ability of the bio-inspired probe to self-penetrate as a function of the distance between the anchor and tip (H). Detailed analysis is presented for probes with H distances equivalent to  $1D_{probe}$ ,  $4D_{Probe}$ , and  $8D_{probe}$ , while select results are provided for probes with other H values to further define trends in the results.



(b)	Input Parameter	Symbol	Value
	Normal Stiffness to Particle Diameter (N/m²)	$k_n/d$	108
	Normal to Shear Stiffness Ratio	$k_n/k_s$	1.5
	Sliding Friction Coefficient	μ	0.4
	Rolling Friction Coefficient	$\mu_{rr}$	0.4
	Ball-probe Friction Coefficient	$\mu_p$	0.3
	Ball-wall Friction Coefficient	$\mu'$	0.1
	Particle Density (kg/m³)	$G_{s}$	2650



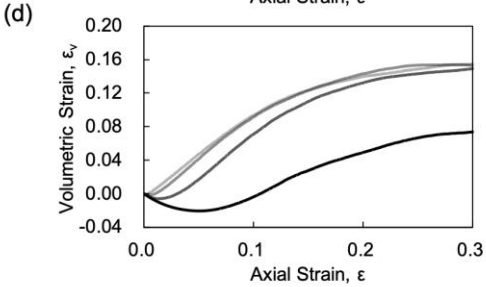


Figure 1. DEM model geometry, parameters and triaxial test calibration. (a) Calibration chamber and probe, (b) simulation parameters, and evolution of (c) deviatoric stresses and (d) volumetric strains with axial strain during triaxial simulations with confining stresses.

During the CP stage, the probe is vertically inserted into the calibration chamber at a constant rate of 0.2 m/s until a penetration depth 0.9 m is achieved. Similar to conventional cone penetration test (CPT),  $q_c$  and  $f_s$  measurements are obtained during penetration. As shown by Chen et al. (2021), the  $q_c$  and  $f_s$  profiles obtained during the CP stage properly reproduce those typically obtained during soundings in medium dense sand.

During the AE stage, an anchor with a length of 0.176m (4  $D_{probe}$ ) located at a distance H from the tip is radially expanded by applying a constant radial velocity of 0.088 mm/s to wall vertices until a target diameter ( $D_{anchor}$ ) of 0.066 mm is achieved

(Figure 2). During this process, the radial anchor  $(P_a)$  and bearing anchor pressures  $(P_b)$  are measured. During expansion, the  $P_a$ values increase to an asymptotic limiting pressure  $(P_L)$ , which has been shown to be consistent with values obtained from classical cavity expansion theory (Chen et al. 2021).

During the SP stage, the anchor is displaced upward while the tip is displaced downward under a velocity-controlled algorithm with force limits. This loading logic is similar to that during an Osterberg pile load test (Osterberg 1989), where the probe section (i.e. anchor or tip) that mobilizes a smaller force is displaced. The detailed logic tree of this motion control algorithm can be found in Chen et al. (2021).

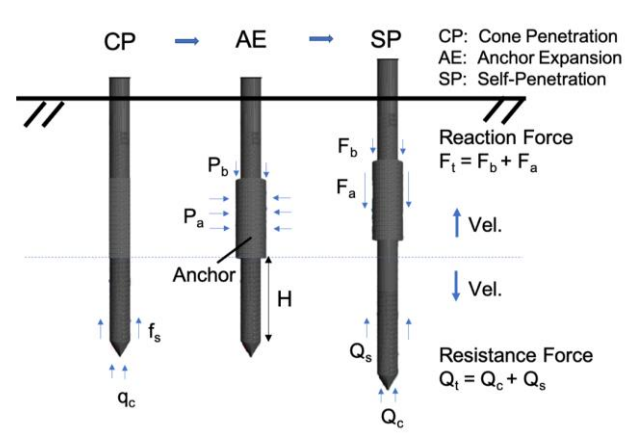


Figure 2. Schematic of three stages of the bio-inspired penetration process in each simulation.

#### RESULTS

The different stages of the self-penetration simulations have vastly different simulation times. Namely, the simulation time of the CP stage is significantly longer than that of the AE and SP stages. To facilitate visualization of the entire self-penetration process in a normalized time series, a normalized timestep  $\overline{N}$  is introduced (Eq. 1). According to the definition of  $\overline{N}$ , values from 0 to 1, 1 to 2, and 2 to 3 correspond to the CP, AE, and SP stages, respectively.

$$\overline{N} = \begin{cases} n/n_1 & (n \le n_1) \\ 1 + (n - n_1)/(n_2 - n_1) & (n_1 < n \le n_2) \\ 2 + (n - n_2)/(n_3 - n_2) & (n > n_2) \end{cases}$$
(1)

where n is the time step and  $n_1$ ,  $n_2$ , and  $n_3$  are the time steps at the end of the CP, AE, and SP stages, respectively.

During the self-penetration (SP) stage, the mobilized reaction and resistance forces are measured, as shown in Figure 2. The anchor friction force  $(F_a)$  and anchor top bearing force  $(F_b)$ compose the total reaction force  $(F_t)$  mobilized by the anchor (Eq. 2-4) while the tip resistance force  $(Q_c)$  and sleeve friction force  $(Q_s)$  compose the total resistance force  $(Q_t)$  (Eq. 5-7).

$$F_a = 2\pi P_a L D_{anchor} f_{anchor}$$
 (2)

$$F_{a} = 2\pi P_{a} L D_{anchor} f_{anchor}$$

$$F_{b} = \frac{\pi}{4} P_{b} (D_{anchor}^{2} - D_{probe}^{2})$$

$$F_{t} = F_{a} + F_{b}$$

$$Q_{c} = \frac{\pi}{4} q_{c} D_{probe}^{2}$$

$$Q_{t} = \pi f_{s} D_{probe}$$

$$Q_{t} = 0 + 0$$

$$F_t = F_a + F_b \tag{4}$$

$$Q_c = \frac{\pi}{4} q_c D_{nrohe}^2 \tag{5}$$

$$Q_t = \pi f_s D_{probe} \tag{6}$$

$$Q_t = \pi J_s \, D_{probe} \tag{6}$$

$$Q_t = Q_c + Q_s \tag{7}$$

where  $P_a$  and  $P_b$  are radial and bearing anchor pressures,  $D_{anchor}$  is the anchor diameter at the end of anchor expansion (0.066 m),  $D_{probe}$  is the initial probe diameter (0.044 m), L is the

anchor length (0.176 m), fanchor is the particle-anchor friction

coefficient, and  $q_c$  and  $f_s$  are the penetration resistance and sleeve friction, respectively. In these simulations,  $f_{anchor}$  has a value equal to the particle-probe friction coefficient.

In this result section, the global-scale analysis is first provided to show the evolution of probe forces and evaluate the probe's self-penetration ability. Then, a geomechanical interpretation of the anchor-tip interactions is provided to complement the results from a meso-scale perspective.

#### Global-scale Analysis

The evolution of the penetration resistance and anchorage reaction forces during the CP, AE, and SP stages are discussed in this section. Figures 3a-3c show the time histories of the force components  $(Q_c, Q_s, F_a, \text{ and } F_b)$  for probes with anchor-tip distances equivalent to  $1D_{probe}$ ,  $4D_{probe}$ , and  $8D_{probe}$ , respectively. Figures 3d-3e present  $F_a$  and  $Q_c$  values at the end of the CP, AE, and SP stages for these simulations along with 4 additional simulations with different *H*.

During the CP stage,  $Q_c$  and  $Q_s$  gradually increase as the probe is inserted into the calibration chamber (Figure 3a-3c). It is noted that the CP stage is identical for three probes. At a penetration depth of 0.9 m ( $\overline{N}$ =1), a  $Q_c$  of about 6.9 kN is mobilized, which is equivalent to a  $q_c$  of 4.5 MPa. This  $q_c$  value is typical of that obtained during field CPT testing in mediumdense sands.

During the AE stage, the anchor forces ( $F_a$  and  $F_b$ ) increase as the anchor is expanded. The values of  $F_a$  during anchor expansion are approximately independent of H (Figure 3d). At the end of the AE stage ( $\overline{N}$ =2), the  $F_a$  and  $F_b$  values are of 6.1 and 1.1 kN, respectively. The corresponding anchor radial limit pressures (i.e. P<sub>L</sub>) are of 835 kPa, which have been shown by Chen et al. 2021 to be consistent with cavity expansion theory simulations in medium-dense sands.

During expansion of the anchor, the magnitude of both resistance forces (i.e.  $Q_c$  and  $Q_s$ ) decreases. Specifically, the  $Q_c$ values decrease from 6.9 kN at the end of the CP stage (show in by a dashed line in Figure 3e) to 3.0 kN, 5.1 kN and 6.2 kN at the end of AE stage for the probes with H = 1  $D_{probe}$ , 4  $D_{probe}$  and 8  $D_{probe}$ , respectively. The results show that a greater decrease in  $Q_c$  and  $Q_s$  occurs for probes with smaller H, as shown in Figure 3e. This indicates that stronger interactions between the anchor and the tip occur in probes with smaller H; further description of these interactions will be provided in the preceding meso-scale analysis.

During the SP stage, the anchor is displaced upward while the tip is displaced downward. As the anchor is displaced upwards, the anchor friction force  $F_a$  tends to decrease (Figure 3d) and the anchor bearing force  $F_b$  tends to increase. This suggests that the radial stress around the anchor decreases, leading to the decrease in  $F_a$ . Simultaneously, this upward displacement leads to the mobilization of bearing resistances at the anchor base, leading to the increase in  $F_b$ . As the probe tip is displaced downward, both  $Q_c$  and  $Q_s$  increase, suggesting the re-mobilization of the tip resistance. It is interesting to note that at the end of SP stage  $(\overline{N}=3)$ , the  $Q_c$  for the three probes remobilize to values close to those at the end of CP stage ( $\overline{N}=1$ ), as shown in Figure 3e. While this remobilization of the penetration resistance suggests that the decrease in  $Q_c$  due to anchor expansion is temporary, it also suggests that the measurements of  $Q_c$  obtained during the SP stage are likely equivalent to undisturbed  $Q_c$  values and thus can be used to estimate soil properties with established correlations for CPT testing.

The self-penetration ability is evaluated here by means of the self-penetration displacement ( $\Delta D$ ), which is defined by Eq.8:

$$\Delta D = \left| \delta_{tip} \right| - \left| \delta_{anchor} \right| \tag{8}$$

where  $\delta_{tip}$  and  $\delta_{anchor}$  are the vertical displacements of the tip and the anchor, respectively. In this way,  $\Delta D > 0$  indicates that self-penetration is achieved while  $\Delta D < 0$  indicates that the anchor is lifted. The motions of the anchor and the tip are velocity-controlled based on force balance, such that the part that mobilizes smaller force is displaced. Figures 4a-4c shows time histories of total reaction and resistance forces during the SP stage for the three probes with H equivalent to 1, 4, and 8  $D_{probe}$ .

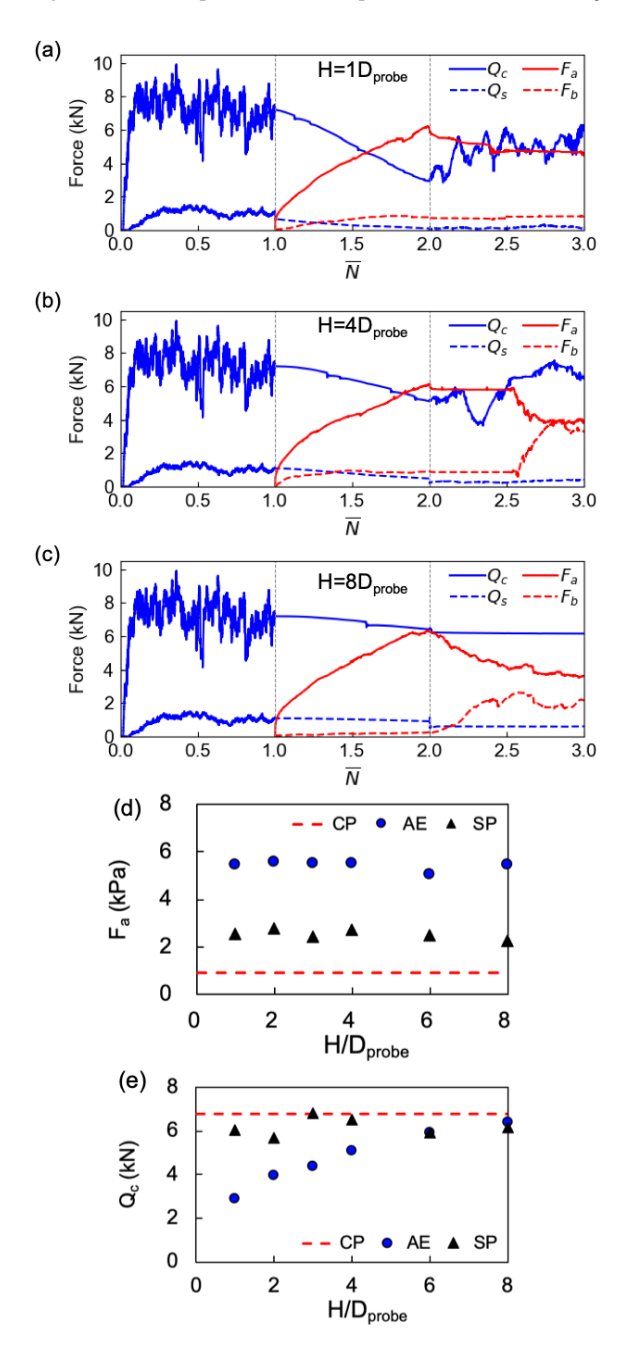


Figure 3. Forces mobilized by the probes with different anchor-tip distances H during the CP, AE, and SP stages. Normalized time histories of reaction and resistance forces for probes with (a)  $H=1D_{probe}$ , (b)  $H=4D_{probe}$ , and (c)  $H=8D_{probe}$  (note:  $\overline{N}$  is the normalized timestep, where  $\overline{N}$   $\in$  [0,1] represents CP stage,  $\overline{N}$   $\in$  [1,2] represents AE stage, and  $\overline{N}$   $\in$  [2,3] represents SP stage). Magnitudes of (d) anchor friction and (e) tip resistance forces at the end of the CP, AE, and SP stages.

Figure 5 presents the evolution of  $\Delta D$  during the SP stage for probes with different H values. The probe with  $H=1D_{probe}$  clearly achieves self-penetration. Because the total anchor force  $F_t$  is

greater than the total resistance force  $Q_t$  (e.g. Figure 4a), the tip continues to move downward while the anchor only displaces upward by a small amount. In contrast, the probe with  $H=8D_{probe}$  does not achieve self-penetration because the  $F_t$  force is smaller than the  $Q_t$  throughout the entire SP stage (e.g. Figure 4c). The probe  $H=4D_{probe}$  is a transitional case, where  $\Delta D$  is initially positive and then decreases to a value slightly smaller than zero. Overall, the results presented in Figures 4 and 5 indicate that the greater reduction in tip resistance induced by the probes with smaller anchor-tip distances result in greater self-penetration displacements.

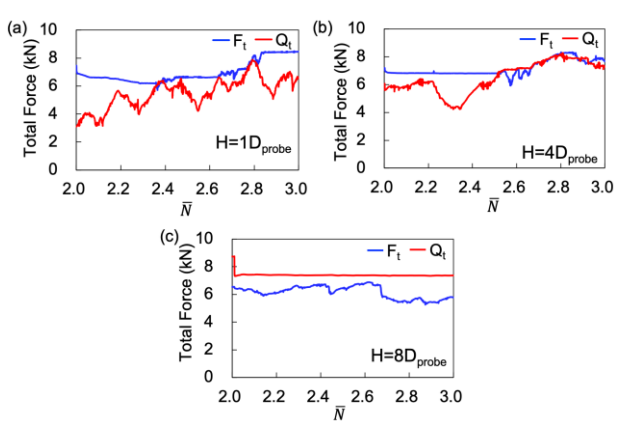


Figure 4. Total reaction and resistance forces for probes with different anchor-tip distances during the SP stage  $(\overline{N} \in [2,3])$ .

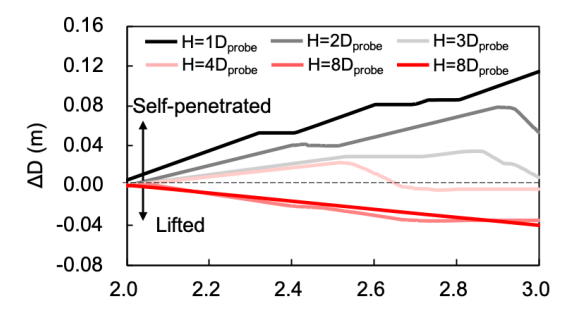


Figure 5. Self-penetration displacements for probes with different anchor-tip distances during the SP stage  $(\overline{N} \in [2,3])$ .

## 3.2 Meso-scale Analysis

This section provides a visualization of the soil stress states during the three simulation stages to provide a geomechanical interpretation of the self-penetration process. Figures 6a-6c present the radial effective stresses ( $\sigma_r'$ ) within the soil surrounding for the probe with an H of 4  $D_{probe}$ . Figures 6d-6f provide visualization of the soil state of stresses by means of crosses, with the length of the crosses being proportional to the magnitude of the principal stress. For each cross, the longer and shorter lines show the relative magnitude and orientation of major and minor soil principal stresses, respectively, at given locations in space.

At the end of the CP stage ( $\overline{N}=1$ ), concentration of radial effective stresses is observed around the tip (Figure 6a). Similar concentrations of radial stress can be seen around the anchor and tip at the end of the AE stage ( $\overline{N}=2$ ) (Figure 6b), and above the anchor and below the tip at the end of the SP stage ( $\overline{N}=3$ ) (Figure 6c). At the end of CP stage, the major principal stresses are oriented perpendicular to the face of the conical tip (Figure 6d). At the end of AE stage, the major principal stresses around the anchor increase in magnitude and rotate to a horizontal orientation which is perpendicular to the expanding anchor's

surface (Figure 6e). The major principal stresses around the tip at the end of AE decrease in magnitude with respect to the end of CP but do not change in orientation. At the end of SP stage, the major principal stresses decrease in magnitude around the anchor and increase in magnitude near the anchor base, where they also rotate to about 60 degrees from horizontal (Figure 6f). Around the probe tip, the major principal stresses have magnitudes and distributions similar to those at the end of the CP stage.

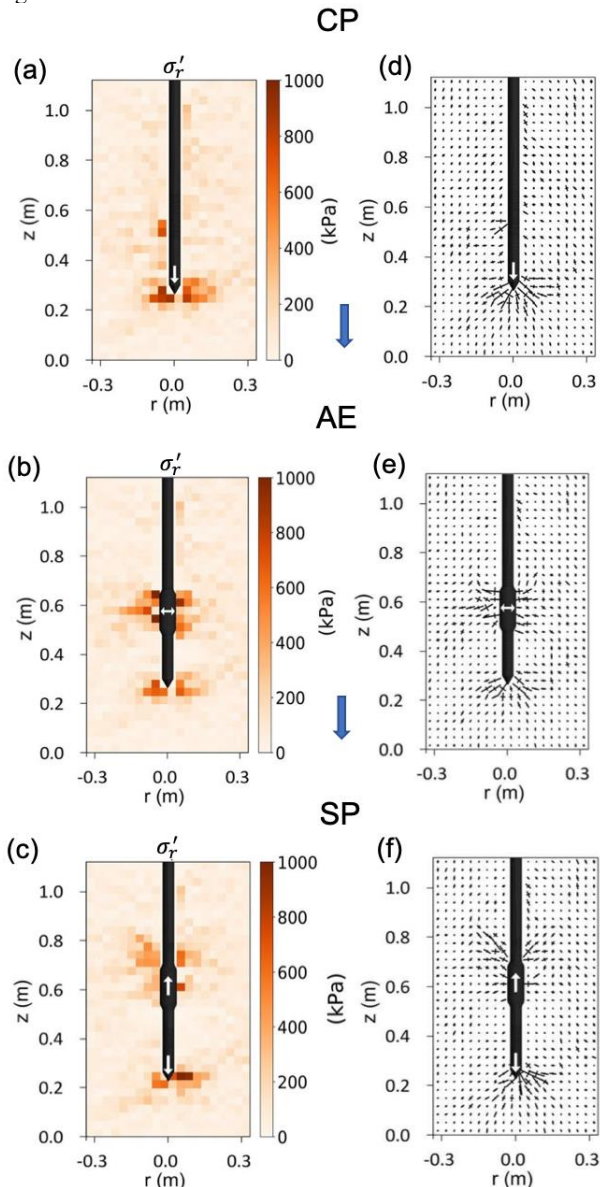


Figure 6. (a–c) radial soil stresses and (d–f) soil stress states for probe with H=4D<sub>probe</sub> at the end of CP ( $\overline{N}$ =1), AE ( $\overline{N}$ =2), and SP ( $\overline{N}$ =3) stages.

Changes of radial effective stress ( $\Delta \sigma'_r$ ) are presented in Figure 7a, 7b, 7e, and 7f to visualize the changes produced as a result of the anchor expansion and self-penetration motions. These results are presented for the probes with H of  $1D_{probe}$  and  $4D_{probe}$ . Figures 7c, 7d, 7g, and 7h show representations of the principal stresses for these two simulations. After the AE stage, the  $\sigma'_r$  increase around the anchor (positive  $\Delta \sigma'_r$ , shown in red) while they decrease around the tip (negative  $\Delta \sigma'_r$ , shown in blue) (Figures 7a-7b). These results explain the mobilization of the radial pressure around the anchor and the reduction in tip resistance force previously described and shown in Figures 3a-3c. The results show that smaller H distances lead to greater decreases in  $\sigma'_r$  around the tip after anchor expansion, thus

leading to greater decrease of  $Q_c$ , as shown in Figure 3e. At the end of the AE stage, the orientations of major principal stresses are similar in the simulations with both probes; however, the magnitudes are smaller near the tip for the probe with a smaller H (Figures 7c-7d).

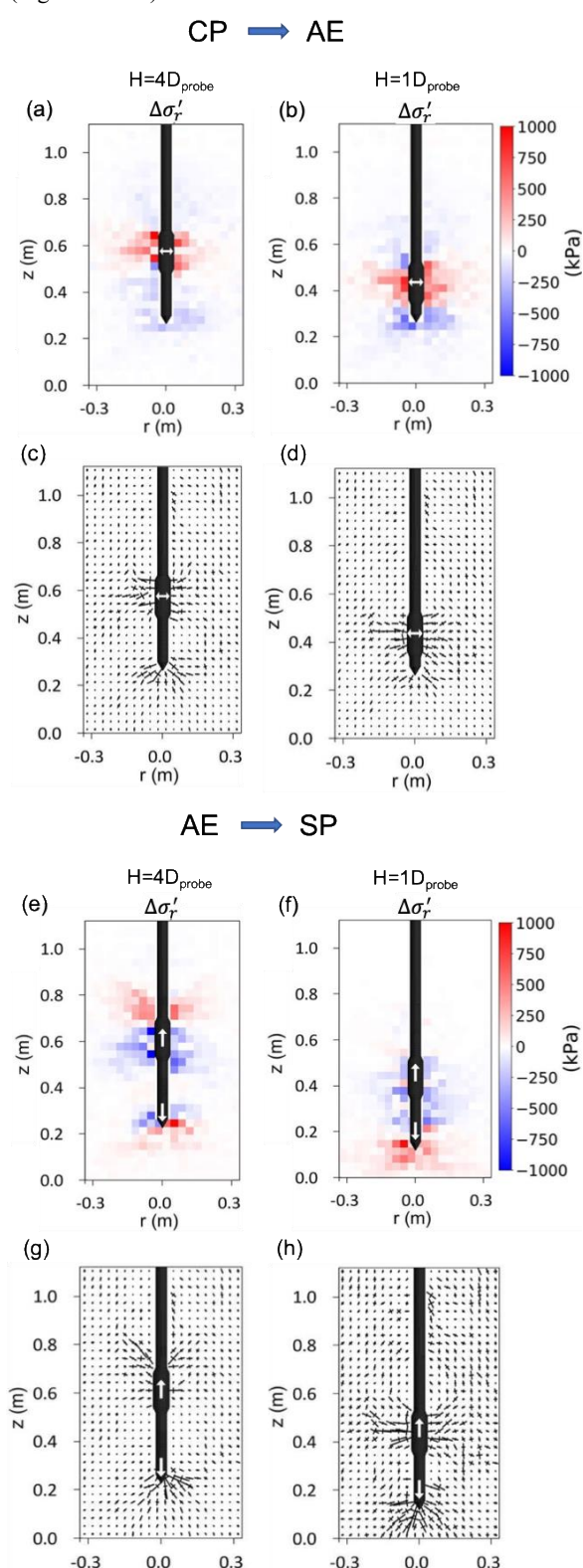


Figure 7. Change of radial stresses and soil stress states for probes with  $H=4D_{probe}$  and  $H=1D_{probe}$ . Radial stress changes (a–b) and soil stress states (c–d) from the end of CP ( $\overline{N}=1$ ) to the end of AE ( $\overline{N}=1$ ); radial stress changes (e–f) and soil stress states (g–h) from the end of AE ( $\overline{N}=2$ ) to the end of SP ( $\overline{N}=3$ ).

r (m)

r (m)

After the SP stage, the  $\sigma'_r$  decreased around the anchor while it increased below the tip (Figures 7e-7f), which is reflected as the decrease in the  $F_a$  force and the remobilization of the  $Q_c$  force, as shown in Figures 3a-3c. The radial stresses increased above the anchor with an H of  $4D_{\text{probe}}$ , while they remained relatively constant for the  $H=1D_{\text{probe}}$  case. These differences are because the shorter anchor only displaced by a small amount due to the greater reduction in penetration resistance observed at the end of AE (Figure 3e). Similarly, large major principal stresses occur above the anchor an H of  $4D_{\text{probe}}$  due to upward motion of the anchor (Figure 7g), while the major principal stresses remain largely unchanged for the H of  $1D_{\text{probe}}$  case (Figure 7h). For both probes, the magnitude and orientation of the principal stresses are similar to those at the end of the CP stage.

#### 4 CONCLUSIONS

This paper presents the results of discrete element modeling simulations of a bio-inspired probe that uses the 'anchor-tip' strategy to self-penetrate in medium-dense coarse-grained soil. The results of simulations on three probes with different anchor-tip distances are used to explore the effect of this parameter on the probe's self-penetration performance and to examine the interactions between the probe's tip and anchor. The main findings of this study include:

- Expansion of the anchor leads to a reduction in the effective stresses below and around the probe's tip and an increase in effective stresses around the probe's anchor. This process produces a reduction in the mobilized tip resistance and an increase in the anchor reaction forces, both of which are necessary for the realization of self-penetration.
- Self-penetration leads to a decrease in the anchor friction force and an increase in the bearing anchor force. The tip resistance is remobilized during self-penetration, which indicates that the decrease due to anchor expansion is temporary; however, this suggests that the values obtained during self-penetration can be used to estimate soil properties with established correlations for CPT testing.
- The distance between the anchor and the tip influences the probe's self-penetration ability, with smaller anchor-tip distances leading to greater reductions in tip resistance during anchor expansion. Self-penetration is achieved when the anchor-tip distance is smaller than 4 times the probe diameter.
- A bio-inspired probe with an appropriate geometry may eliminate the need of heavy equipment to perform in-situ penetration soundings such as CPT, PMT, and DMT in medium-dense coarse-grained soil.

The presented simulations are for limited conditions. Future studies should address the effects of other anchor configurations, such as the anchor length, expansion magnitude, and friction coefficient, as well as alternate sequences of motion and a wider range of soil properties and stress levels to provide a full evaluation of the self-penetration process. In addition, future research should provide experimental validation of the reported trends through laboratory and field testing.

## 5 ACKNOWLEDGEMENTS

This material is based upon work supported in part by the Engineering Research Center Program of the National Science Foundation under NSF Cooperative Agreement No. EEC-1449501) and by the NSF Award No. 1942369. Any opinions, findings, and conclusions or recommendations expressed in this material are those of the author(s) and do not necessarily reflect those of the National Science Foundation.

#### 6 REFERENCES

Arroyo M., Butlanska J., Gens A., Calvetti F., and Jamiolkowski M. 2011. Cone penetration tests in a virtual calibration chamber. *Geotechnique*, 61(6): 525-31.

- Borela R., Frost J.D., Viggiani G., and Anselmucci, F. 2021. Earthworminspired robotic locomotion in sand: an experimental study with Xray tomography. Géotechnique Letters, 11(1): 66-73.
- Burrall M., DeJong J.T., Martinez A., and Wilson D.W. 2020. Vertical pullout tests of orchard trees for bio-inspired engineering of anchorage and foundation systems. *Bioinspiration & Biomimetics*, 16(1): 016009.
- Ciantia M.O., Arroyo M., Butlanska J., and Gens A. 2016. DEM modelling of cone penetration tests in a double-porosity crushable granular material. *Computers and Geotechnics*, 73: 109-127.
- Cortes D. and John S. 2018. Earthworm-inspired soil penetration. *In Proceedings of the 1st Biomediated and Bioinspired Geotechnics (B2G) Conference*. Atlanta.
- Chen Y., Khosravi A., Martinez A., and DeJong J. 2021. Modeling the Self-Penetration Process of a Bio-Inspired Probe in Granular Soils. In press in *Bioinspiration and Biomimetics*.
- Dorgan K.M. 2015. The biomechanics of burrowing and boring. *Journal of Experimental Biology*, 218(2): 176–183.
- Gans C. 1973. Locomotion and burrowing in limbless vertebrates. Nature, 242(5397): 414-415.
- Khosravi A., Martinez A., DeJong J.T., and Wilson D. 2018. Discrete element simulations of bio-inspired self-burrowing probes in sands of varying density. In Proceedings of the Biomediated and Bioinspired Geotechnical (B2G) Conference, Atlanta, GA, 12–13.
- Khosravi A., Martinez A., and DeJong J.T. 2020. Discrete element model (DEM) simulations of cone penetration test (CPT) measurements and soil classification. *Canadian Geotechnical Journal*, 57(9): 1369–1387.
- Mayne P.W. 2007. Cone penetration testing (Vol. 368). Transportation Research Board.
- Mallett S.D., Matsumura S., and Frost D. 2018. Additive manufacturing and computed tomography of bio-inspired anchorage systems. *Géotechnique Letters*, 8(3): 219-225.
- Martinez A., Palumbo S., and Todd B.D. 2019. Bioinspiration for anisotropic load transfer at soil–structure interfaces. *Journal of Geotechnical and Geoenvironmental Engineering*, 145(10): 04019074.
- Martinez A., DeJong J.T., Jaeger R.A., and Khosravi A. 2020. Evaluation of self-penetration potential of a bio-inspired site characterization probe by cavity expansion analysis. *Canadian Geotechnical Journal*, 57(5): 706-716.
- Martinez A., DeJong J., et al. 2021. Bio-inspired geotechnical engineering: principles, current work, opportunities and challenges. *Geotechnique*, http://doi.org/10.1680/jgeot.20.P.170.
- Meijer G.J., Wood D.M., Knappett J.A., Bengough A.G., and Liang T. 2019. Root branching affects the mobilization of root-reinforcement in direct shear. *In E3S Web of Conferences*, 92: 12010.
- O'Hara K.B. and Martinez A. 2020. Monotonic and Cyclic Frictional Resistance Directionality in Snakeskin-Inspired Surfaces and Piles. *Journal of Geotechnical and Geoenvironmental Engineering*, 146(11): 04020116.
- Osterberg J. 1989. New device for load testing driven piles and drilled shafts separates friction and end bearing. *In Piling and Deep Foundations: Proceedings of the International Conference on Piling and Deep Foundations*, London, 1: 421.
- Purdy C., Raymond A.J., DeJong J.T., and Kendall A. 2020, February. Life Cycle Assessment of Site Characterization Methods. *In Geo-Congress* 2020, 80–89. Reston, VA: American Society of Civil Engineers.
- Raymond A.J., Tipton J.R., Kendall A., and DeJong J.T. 2020. Review of impact categories and environmental indicators for life cycle assessment of geotechnical systems. *Journal of Industrial Ecology*, 24(3): 485–499.
- Sadava D.E., Hillis D.M., Heller H.C., and Berenbaum M. 2009. *Life:* the science of biology (Vol. 2). Macmillan.
- Stutz H.H. and Martinez A. 2021. Directionally dependent strength and dilatancy behavior of soil–structure interfaces. *Acta Geotechnica*, 28: 1-16.
- Tao J., Huang S., and Tang Y. 2020. SBOR: a minimalistic soft self-burrowing-out robot inspired by razor clams. *Bioinspiration and Biomimetics*, 15(5): 1–22.
- Wensrich C.M. and Katterfeld A. 2012. Rolling friction as a technique for modelling particle shape in DEM. Powder Technology, 217: 409-417
- Zhang N., Arroyo M., Ciantia M.O., Gens A., and Butlanska J. 2019. Standard penetration testing in a virtual calibration chamber Computers and Geotechnics, 111: 277-289.